Supporting Information

for

Investigations on the Field Dependency of Proton and Charge Transfer Kinetics in Atmospheric Pressure Corona Discharge Sources

Christoph Schaefer,*,‡,a Alexander Haack,*,‡,a Charlotte Hellwig,a Jannik Wuttke,a and Stefan Zimmermanna

a Leibniz University Hannover, Institute of Electrical Engineering and Measurement Technology, Department of Sensors and Measurement Technology, Appelstr. 9A, 30167 Hannover, Germany

*Corresponding Authors: schaefer@geml.uni-hannover.de, haack@geml.uni-hannover.de
‡ These authors contributed equally.

Table of contents

Section S1. Instrumental Setups

To accurately determine the reaction rate coefficients for proton transfer of the model analytes with $H_3O^+(H_2O)_n$ and charge transfer with $NO^+(H_2O)_m$, it is essential to selectively provide these reactant ion species in high purity. Therefore, a new reactant ion source is developed in this work. The developed reactant ion source selectively provides a single reactant ion species in high purity, utilizing a setup based on printed circuit boards (PCBs), as schematically shown in Figure 1 of the main manuscript. Applying a high voltage U_{GD} between a stainless-steel needle (G1947-20029, Agilent Technologies, USA) and a home-built stainless-steel hollow electrode leads to the glow discharge, initiating reactant ion formation. The serial resistor R_{Ser} limits the discharge current I_D. The needle is mounted gas-tight is electrically connected to a standard 1/4" stainless-steel tube. The tube docks into a PCB-mounted fitting (SS-TCW-VL4-A6, FITOK GmbH, Germany), allowing adjustment of electrode distance while maintaining vacuum conditions.

Similar to earlier PCB-based IMS designs, the ion source is built from four individual PCBs, with one on each side,[1,2] bonded together to maintain vacuum conditions. Applying the ion source voltage U_{IS} between the hollow electrode and the end of the ion source (interface) establishes the reduced ion source field strength E_{IS}/N that transports ions toward the interface. In this region, conductor tracks on the PCB act as electrodes, analogous to IMS drift rings. Each electrode is connected to an external resistor network, where the electric potentials are determined by the voltage divider of the resistor network. The chosen E/N influences the effective temperature of primary and reactant ions, affecting their cluster formation with neutral molecules. Hence, this parameter is critical for selecting different reactant ion species by shifting the chemical equilibrium of the whole reaction system in favour of the desired ion species. It also controls the drift velocities and residence times of reactant ions in the ion source. These reaction times must be sufficient to reach equilibrium before the ions exit the ion source.

A mass flow controller (F-200DC-ABD, Bronkhorst Nord, Germany) supplies a doped source gas to select specific reactant ion species with a constant flow rate of 12 mL/min (related to 1013.25 hPa and 293.15 K). The ion source is evacuated by a diaphragm pump (MVP 040-2, Pfeiffer Vacuum, Germany), with a capacitive pressure gauge (CMR 362, Pfeiffer Vacuum, Germany) monitoring the operating pressure. Key operating parameters for the ion source are detailed in Table S1. The reduced field strength and neutral gas composition for providing H_3O^+ (H_3O^+ mode) and NO^+ (NO^+ mode) were optimised in a parameter study to ensure maximum relative intensity of the selected reactant ion species in both operating modes.

Table S1. Operating parameter of the newly developed ion source.

Parameter	Value	
Operating mode	H_3O^+ mode	NO^+ mode
Voltage U_{GD}	700 V	1300 V
Discharge current I_D	10 – 15 µA	2 – 4 mA
Serial resistor R_{Ser}	200 kΩ	200 kΩ
Reduced ion source field strength E_{IS}/N	20 Td	80 Td
Neutral gas	Air	Air
Water concentration	4,000 ppm_V	70 ppm_V
Operating pressure	8 mbar	8 mbar
Operating temperature	298 K	298 K
Ion source length	70 mm	70 mm

The mass spectra obtained by coupling the developed ion source to the PTR-QMS 300, as shown in Figure S1, demonstrate that both $H_3O^+(H_2O)_n$ and $NO^+(H_2O)_m$ can be selectively formed. In the NO^+ mode, there are only minor contributions from H_3O^+ and its monohydrate, and NO^+ does not significantly form hydrates. Similarly, in the H_3O^+ mode, almost no interfering ion species, such as NO^+, are observed, although H_3O^+ forms hydrates with up to two water molecules. However, this is not expected to significantly interfere with ion-molecule reaction investigations. For such detailed investigations, the ion source will be coupled to a standalone HiKE-IMS. The operating parameters of the ion source, including the reduced ion source field strength, will be kept constant to ensure consistent production of a specific reactant ion species. In the reaction region, rather than using the doped source gas, only the sample gas containing analyte molecules will be introduced, so the reactant ions react solely with neutral analytes. During experiments on ion-molecule reactions, the reduced field strength in the reaction region varies and differs from that in the ion source. When the reduced field strength changes between regions, a new cluster equilibrium quickly establishes upon transferring the reactant ions to the reaction region. This shift in cluster equilibrium is typically fast compared to residence times in the reaction and drift region,[3,4] so hydration in the ion source is not expected to significantly affect ion chemistry in the reaction region. These results demonstrate that the developed ion source can selectively produce $H_3O^+(H_2O)_n$ and $NO^+(H_2O)_m$, providing the instrumental basis for detailed investigations of ion-molecule reactions at various reduced field strengths.

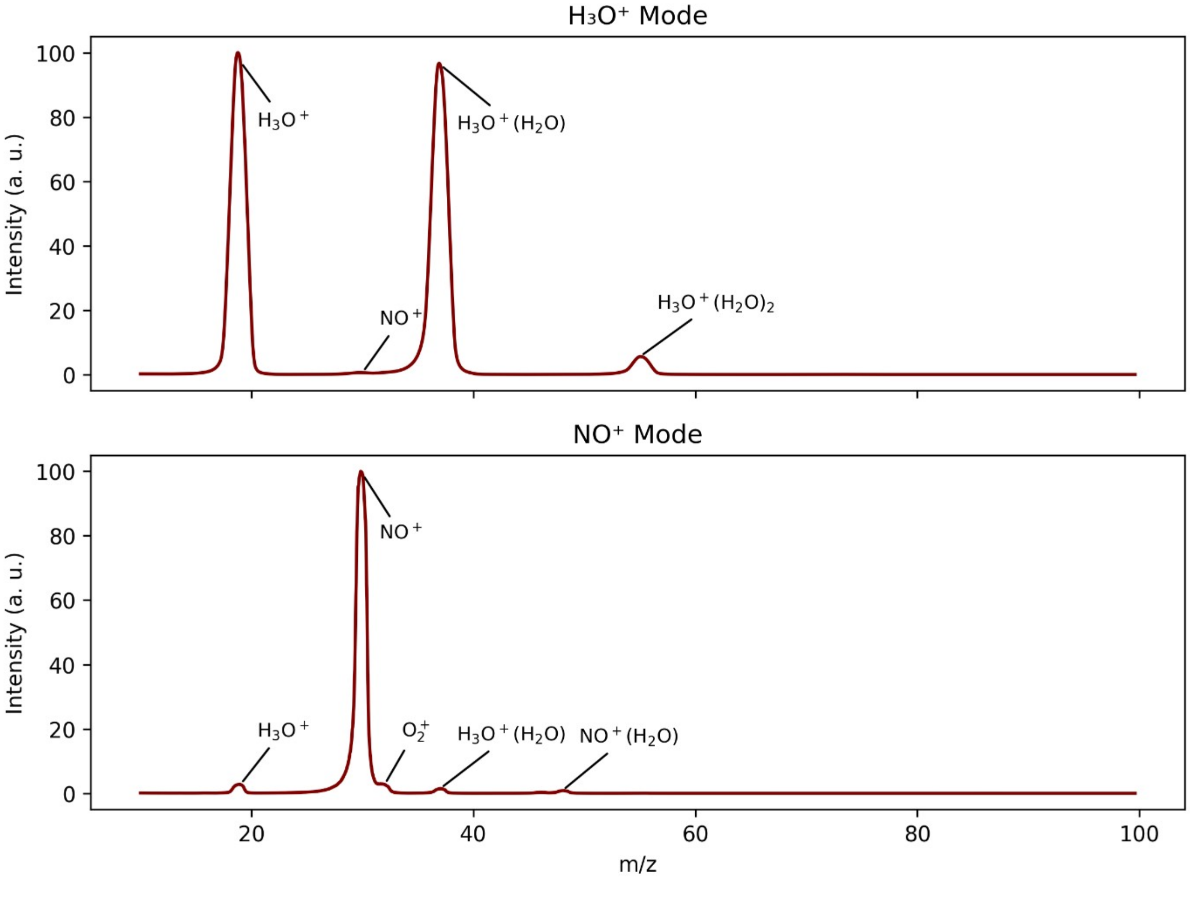

Figure S1. Mass spectra of the reactant ions generated from the glow discharge ion source a) in the H_3O^+ mode at 20 Td in humified air (1,000 ppm_V H_2O) and b) in the NO^+ mode at 80 Td in dry air, determined by coupling the ion source to a PTR-QMS 300. The ion source parameters are detailed in Table S1. All other operating parameters according to Table S2 and Table S3.

To reliably identify the formed ions, the developed ion source will first be coupled to a quadrupole mass spectrometer (PTR-QMS 300, Ionicon Analytik, Austria). This coupling allows for the unambiguous identification of the formed reactant ion species based on their mass-to-charge ratio and enables the investigation of cluster size distributions. Additionally, the low operating pressure of the PTR-QMS 300 and the intermediate pressure stage between the ion source and the mass spectrometer ensure that the formed ions do not react significantly with neutral analyte molecules after exiting the ion source. Such a reaction could occur if the ion source is coupled with a HiKE-IMS, consisting of a reaction and drift region, potentially leading to discrepancies between the analysed ion population and the ion population formed by the ion source.

For coupling of the ion source to the PTR-QMS 300, as schematically shown in Figure S2(a), the ion source and the reaction region of the PTR-QMS 300 are removed to mount the developed ion source *via* its interface to the first pinhole to the MS. This coupling operates without further modifications, using the operating parameters summarised in Table S2.

After characterising the developed ion source using the PTR-QMS 300, the ion source is coupled to a HiKE-IMS, as shown in Figure S2(b). This instrumental setup is used to conduct experiments on the reaction kinetics of proton transfer and charge transfer. In this setup, the reactant ions formed in the ion source ionise the neutral analytes introduced by the sample gas in a reaction region. All formed ions are eventually analysed by their ion mobility in a drift region. The reduced field strengths in the ion source, reaction region, and drift region can be separately adjusted to control reactant ion formation, ionisation of neutral analytes, and their separation.

The experimental setup requires a doped source gas, a sample gas, and a drift gas. Two mass flow controllers (F-200DV-ABD, Bronkhorst Nord, Germany) control the doped source gas and drift gas flow, both with a constant flow rate of 12 mL/min (related to a pressure of 1013.25 hPa and 293.15 K). Drift gas is introduced at the end of the drift region, while the doped source gas is introduced to the ion source as detailed in the main manuscript. The sample gas is passively introduced by a 1/16” capillary with an internal diameter of 250 µm due to the pressure difference between the reaction region of the HiKE-IMS (8 mbar) and the gas mixing setup operated at approximately 1000 mbar. By adjusting the length of the sample gas capillary, the sample gas flow rate is set to 11.7 mL/min. The doped source gas, sample gas, and drift gas are evacuated at the interface between the ion source and the reaction region by two diaphragm pumps (MVP 040-2, Pfeiffer Vacuum, Germany). This ensures the spatial separation between reactant ion formation and ionisation of neutral analytes. Table S3 summarizes the operating parameters of the coupling between the ion source and HiKE-IMS.

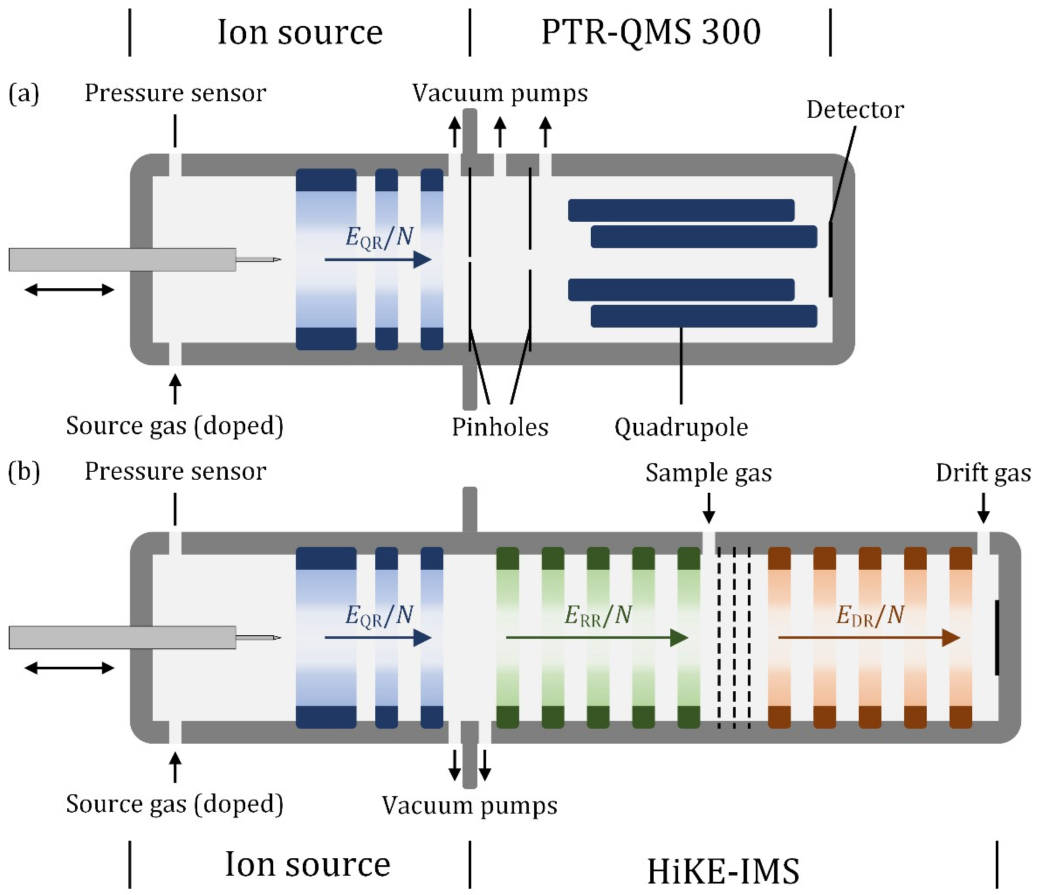

Figure S2. Schematic instrumental setup a) of the coupling between ion source and PTR-QMS 300 with intermediate pressure stage and b) of the coupling between ion source and HiKE-IMS.

Table S2. Operating parameters of the coupling between ion source and PTR-QMS 300.

Parameter	Value
Operating temperature	303 K
Operating pressure ion source	8 mbar
Operating pressure PTR-QMS 300	$7 \cdot 10^{-5}$ mbar
Pinhole potential PTR-QMS 300	175 V[a]
Reference potential PTR-QMS 300	150 V[a]
Cathode potential PTR-QMS 300	80 V[a]
Focus potential PTR-QMS 300	144 V[a]
Field axis potential PTR-QMS 300	143 V[a]
Extraction potential PTR-QMS 300	100 V[a]

[a] Electric potential relates to ground potential (0 V).

Table S3. Operating parameters of the coupling between ion source and HiKE-IMS.

Parameter	Value
Length reaction region	50 mm
Length drift region	306.5 mm
Reduced reaction field strength	20 – 120 Td
Reaction region voltage	200 – 1200 V
Reduced drift field strength	120 Td
Drift region voltage	7000 V
Ion gate opening time	1 µs
Flow rate sample gas	11.7 mL/min[a]
Flow rate drift gas	12 mL/min[a]
Operating temperature	303 K
Operating pressure	8 mbar
Assumed water volume fraction	70 ppm_V

[a] All gas flow rates relate to a pressure of 1013.25 hPa and 293.15 K.

Section S2. Formal kinetic treatment of proton and charge transfer reactions

For the simplified ionisation reaction scheme,

$$RI^{+} + A\xrightarrow{k_1}[RI + A]^{+}\#(S1)$$

$$[RI + A]^{+}\xrightarrow{k_{-1}}RI^{+} + A\#(S2)$$

$$[RI + A]^{+}\xrightarrow{k_2}RI + A^{+}\#(S3)$$

We can derive a first-order kinetic for the formation of ionised analyte molecules. Crucial is the assumption that the reaction complex, $[RI+A]^+$ is short-lived and thus, that its concentration is in a steady state:

$$0 = \frac{d[[RI + A]^{+}]}{dt} =+ k_1[RI^{+}][A] - k_{-1}[[RI + A]^{+}] - k_2[[RI + A]^{+}]\#(S4)$$

Which can be rearranged to

$$[[RI + A]^{+}] = \frac{k_1[RI^{+}][A]}{k_{-1} + k_2}\#(S5)$$

The rate equation for the formation of the ionised analyte reads

$$\frac{d[A^{+}]}{dt} = k_2[[RI + A]^{+}]\#(S6)$$

Where we can now substitute in Eq. (S5) yielding:

$$\frac{d[A^{+}]}{dt} = \frac{k_2k_1[A]}{k_{-1} + k_2}[RI^{+}]\#(S7)$$

If we further assume that $[A] \gg [RI^{+}]$, we can assume pseudo first-order with respect to $[A]$, *i.e.*, set $[A] = const$, and yield a total rate of

$$\frac{d[A^{+}]}{dt} =- \frac{d[RI^{+}]}{dt} = k_{tot}[RI^{+}]\#(S8a)$$

$$k_{tot} = \frac{k_2k_1[A]}{k_{-1} + k_2}\#(S8b)$$

Depending on the situation, this can be further simplified. If $k_2 \gg k_{-1}$, *i.e.*, the decomposition of the reaction complex towards the products is much faster than the back reaction, the total rate becomes equivalent to the association rate:

$$k_{tot} \approx k_{lim2} = k_1[A]\#(S9)$$

Conversely, if the reaction back to the reactants is strongly favoured, *i.e.*, $k_2 \ll k_{-1}$, we obtain a total rate that is basically the decomposition rate of the reaction complex towards the reactants times the equilibrium constant for the initial association of the reaction complex.

$$k_{tot} \approx k_{lim1} = k_2\frac{k_1[A]}{k_{-1}} = k_2K_{ass}\#(S10)$$

Note that K_{ass} can also be described by thermochemical data:

$$K_{ass} = \exp\left(-\frac{\Delta G_{ass}}{k_B T}\right)\#(S11)$$

In both limiting cases, the rate equation Eq. (S8a) can be integrated, yielding:

$$[RI^+]_t = [RI^+]_{t=0} \cdot e^{-k_{tot}t}\#(S12a)$$

$$[A^+]_t = [RI^+]_{t=0} \cdot \left(1 - e^{-k_{tot}t}\right)\#(S12b)$$

Or using a bimolecular rate, k_{obs}, we get:

$$[RI^+]_t = [RI^+]_{t=0} \cdot e^{-k_{obs}t[A]}\#(S13)$$

which is Eq. (8) from the main manuscript.

Section S3. Reaction Schemes and Structures for the Modelling

Here we describe the full reaction schemes used for the modelling of the proton transfer (PT) and charge transfer (CT) reactions. Additionally, we show exemplary structures of the found complexes.

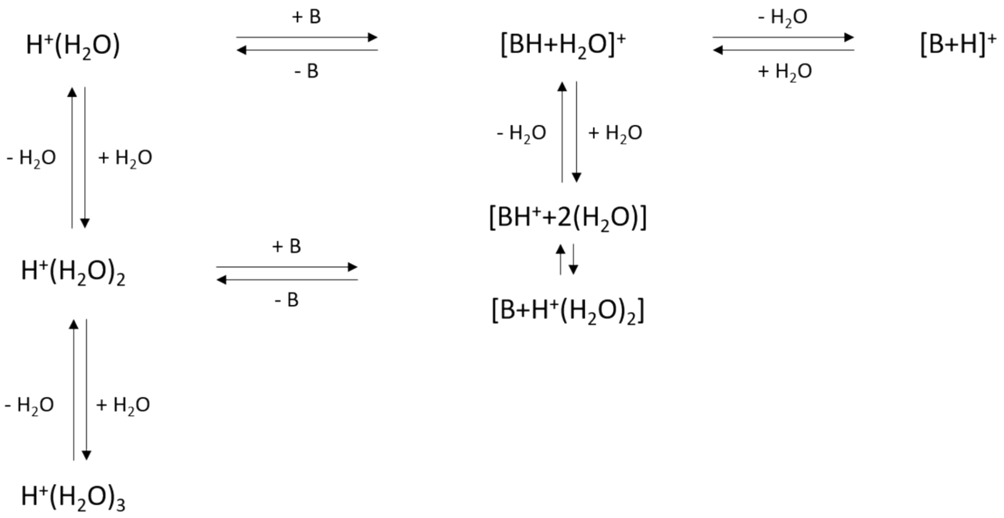

Figure S3: Full reaction scheme used for the modelling of the proton transfer reactions. Scheme shown for benzene (B) but is the same for toluene and p-xylene. Note that the reaction complex containing only one water has only one minimum structure, while the reaction complex containing two water molecules has two.

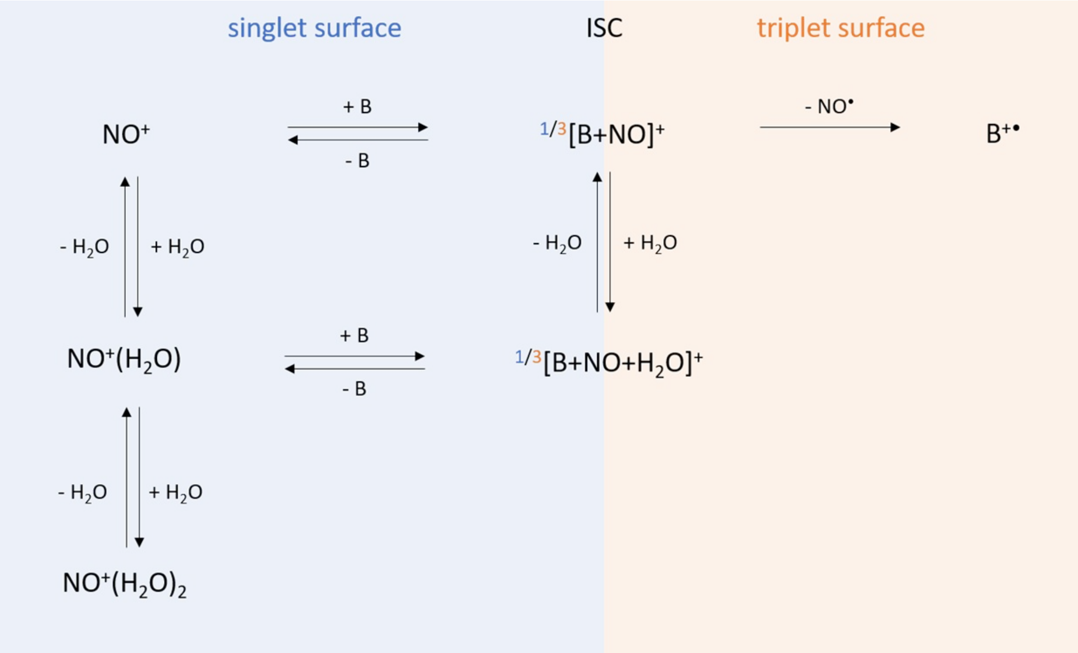

Figure S4: Full reaction scheme used for the modelling of the charge transfer reactions. Scheme shown for benzene (B) but is the same for toluene and p-xylene. The reaction occurs on a diabatic surface, which can be approximated by a singlet surface on the reactant and a triplet surface on the product side. Consequently, the reaction complexes can undergo an intersystem crossing (ISC) to change their spin state from singlet to triplet (and back).

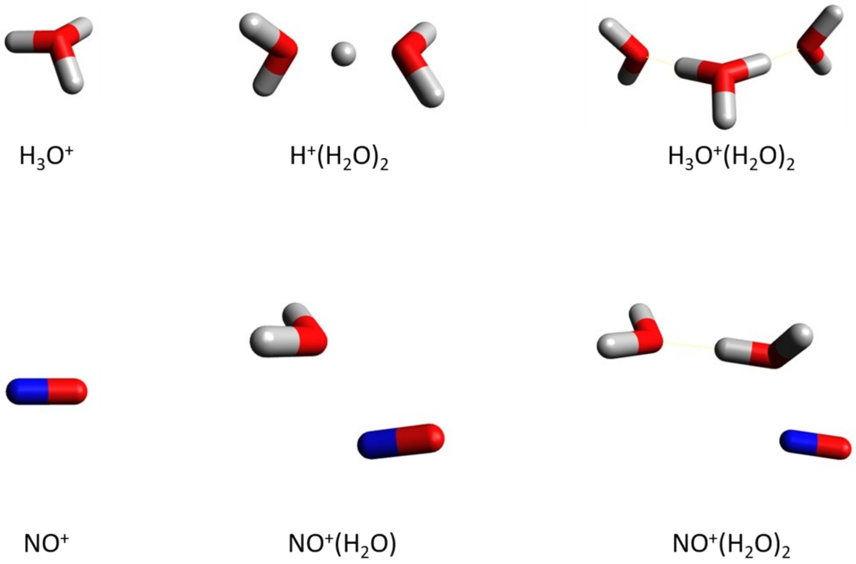

Figure S5: Structures of the reactant ions $H_3O^+(H_2O)_n$ and $NO^+(H_2O)_m$ for n=0,1,2 and m=0,1,2 as optimised on the ωB97X-D3(BJ)/def2-TZVPP level of theory.

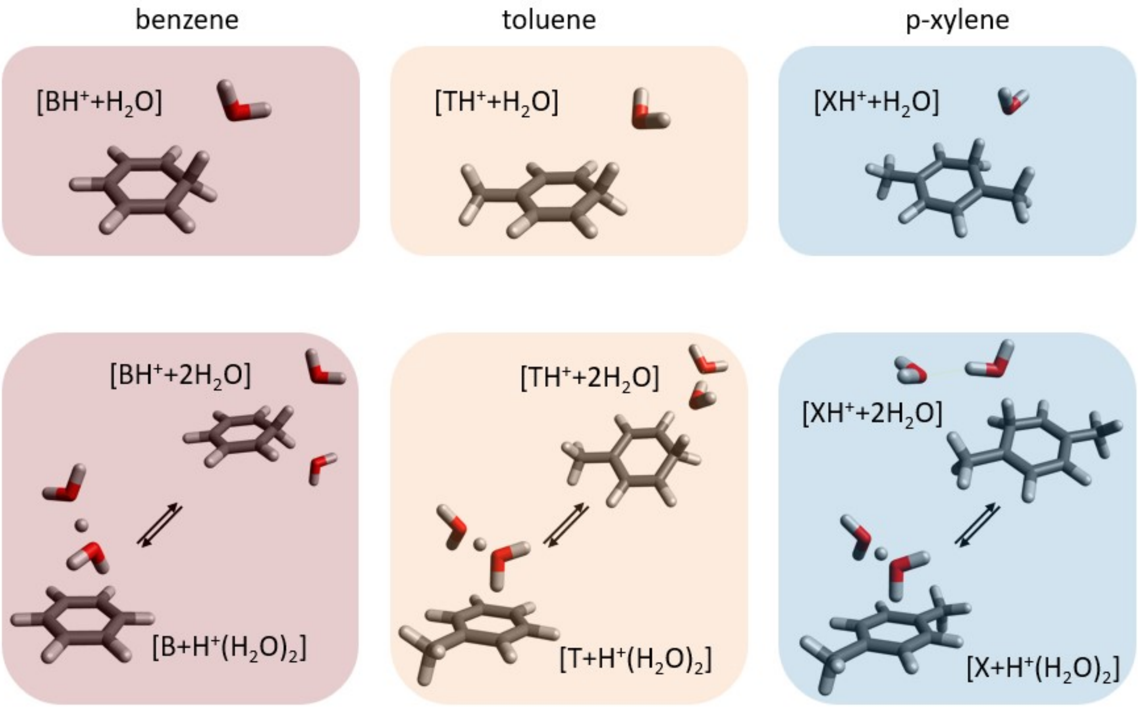

Figure S6: Structures of the reaction complexes of the proton transfer reactions for benzene, toluene and p-xylene as optimised on the ωB97X-D3(BJ)/def2-TZVPP level of theory.

The charge transfer reactions of NO^+ to the three model analytes proceeds on a diabatic potential energy surface as the reactants (NO^+ and the neutral analytes, A) can be described by a singlet state, while the reaction products ($NO^\bullet$ and $A^{\bullet+}$) can be well described by a triplet state. Indeed, we found a stable reaction complex $^{1/3}[NO + A]^+$ in both spin states as shown in Figure S7. The binding of the reaction complex in the singlet state can be well described by a π-π-interaction of the two fragments with the charge being mainly localised at the NO, see Figure S8. Conversely, the binding of the reaction complex in the triplet state shows a much longer analyte-NO bond, with the singly occupied orbital of the NO pointing towards the singly occupied *p*-orbital of the analyte. Here, population analysis shows a spin density of 1 at each fragment with the charge localised at the analyte, representing the charge transfer product. As the bond order of NO^+ is higher than that of $NO^\bullet$ (see Figure S9 for the molecular orbital diagram), the bond distance in NO^+ is significantly shorter as compared to $NO^\bullet$ (1.068 Å compared to 1.152 Å according to our modelling). The geometry of the analyte does not change significantly. Thus, the crossing of the singlet and triplet surface can be well represented by the analyte-NO distance, represented by a Morse potential, and the N-O bond distance, represented by a harmonic oscillator potential, which is shown in Figure S8. The parameters for the Morse and harmonic oscillator potentials were obtained from the vibrational frequencies connected to these coordinates.

Figure S8 shows that the minimum energy crossing point (MECP) of the two surfaces is only slightly higher in energy than the triplet reaction complex and that the respective Morse potential is very shallow. In particular, starting at the energy of the reactants (blue dashed line as the limit of the singlet Morse potential), only a small amount of kinetic energy is required to exit the diabatic surface through the triplet channel, *i.e.*, ionising the products. Keep in mind, that the triplet limit (red dashed line) for toluene and *p*-xylene is even lower due to their higher ionisation energies. Thus, we speculate that the triplet reaction complex is not actually stable: Upon a collision of NO^+ and the neutral analyte, the singlet reaction complex $^1[NO^+ + A]$ is formed and can easily occupy areas of the configurational space that correspond to the triplet complex, that, however, is stable enough to increase the phase-space density in this region significantly. As a consequence, we model the rate coefficients towards the singlet and triplet exit channel as loose TSs from the singlet complex.

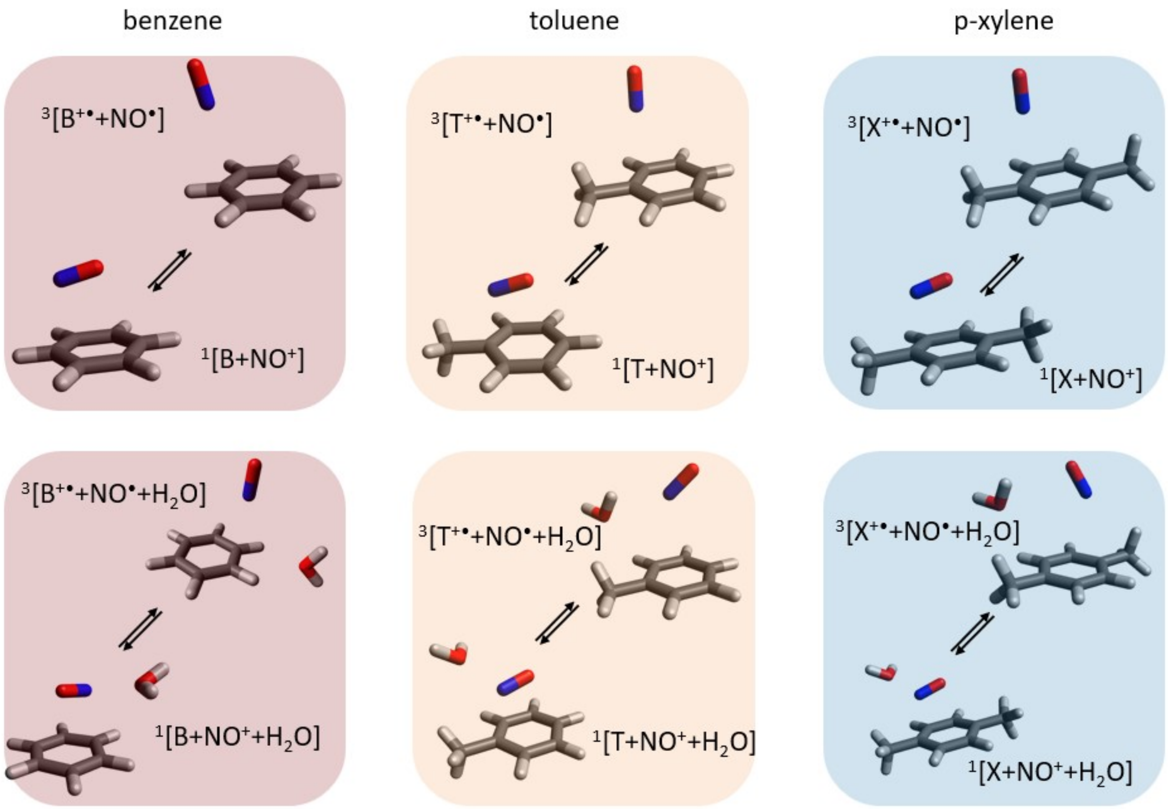

Figure S7: Structures of the reaction complexes of the charge transfer reactions for benzene, toluene and p-xylene as optimised on the ωB97X-D3(BJ)/def2-TZVPP level of theory.

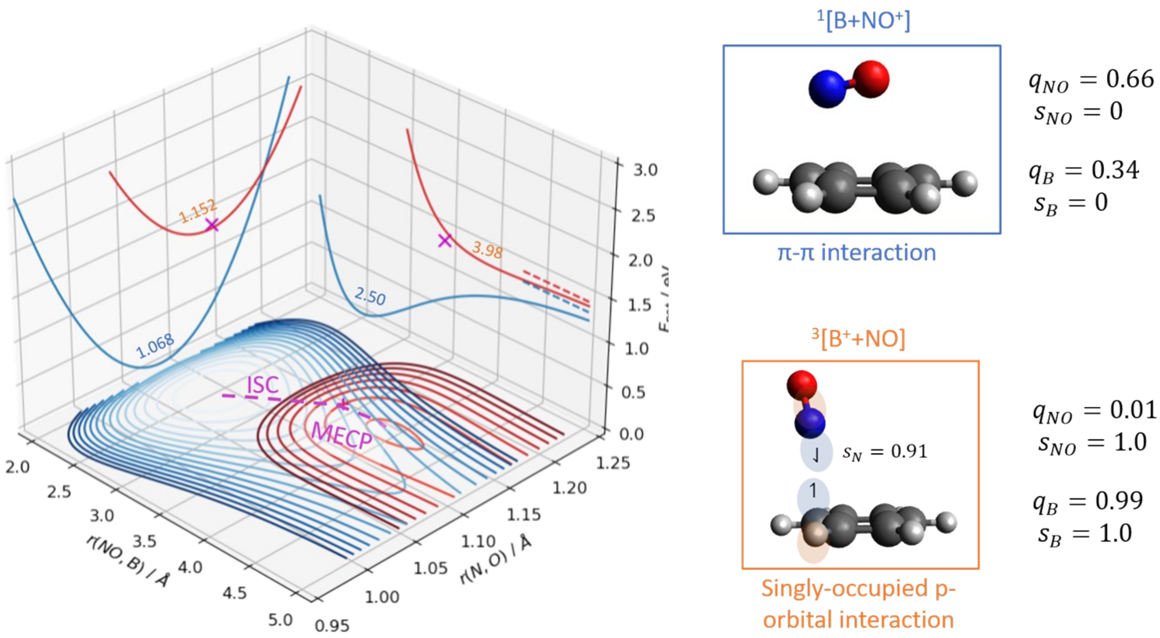

Figure S8: Details of the intersystem crossing (ISC) process. Left: Projections of the two crossing surfaces (singlet: blue, triplet: orange) with respect to the N-O (harmonic potential) and NO-B (Morse potential) distances. Force and distance parameters obtained on the ωB97X-D3(BJ)/def2-TZVPP level of theory. Compared to the singlet configuration, the triplet shows a longer N-O bond and a much weaker NO-B binding potential. The ISC pathway is shown in pink and shows that an elongation of both the N-O bond and the NO-B distance occurs. Right: Geometries and Mulliken charge/spin densities of the two structures. In the singlet case, the charge (q) is mostly localised at the NO^+ with no total spin density (s) on either fragment. Conversely, in the triplet state, the charge is fully localised on the benzene while each fragment shows a total spin density of one, highlighting the biradical character.

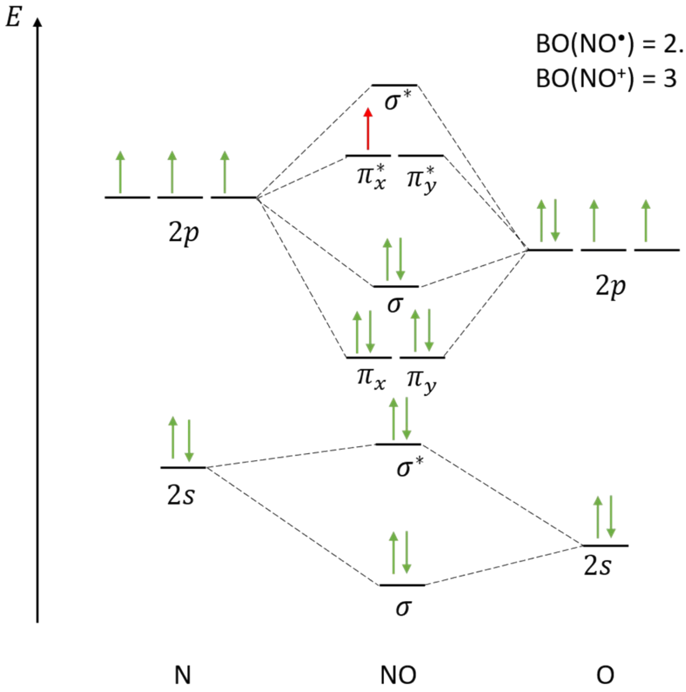

Figure S9: Molecular orbital (MO) diagram of NO in its neutral ($NO^{\bullet}$, including red electron) and cationic (NO^{+}, excluding red electron) form. Because the free electron occupies an antibonding orbital, the total bond order of neutral NO is 2.5, whereas removal of this electron yields a total bond order of 3. Consequently, the bond is stronger in case of NO^{+}, which is also reflected in the bond distances (1.068 Å for NO+ and 1.152 Å for $NO^{\bullet}$ as computed on the ωB97X-D3(BJ)/def2-TZVPP level of theory).

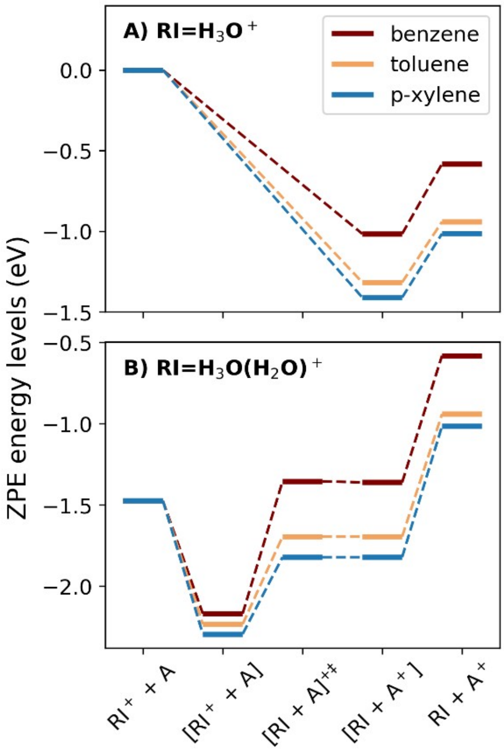

Figure S10: Computed zero-point energy levels for the reactants, products, and intermediate reaction complexes of proton transfer from H_3O^+ and $H_3O^+(H_2O)$ with benzene, toluene, and p-xylene.

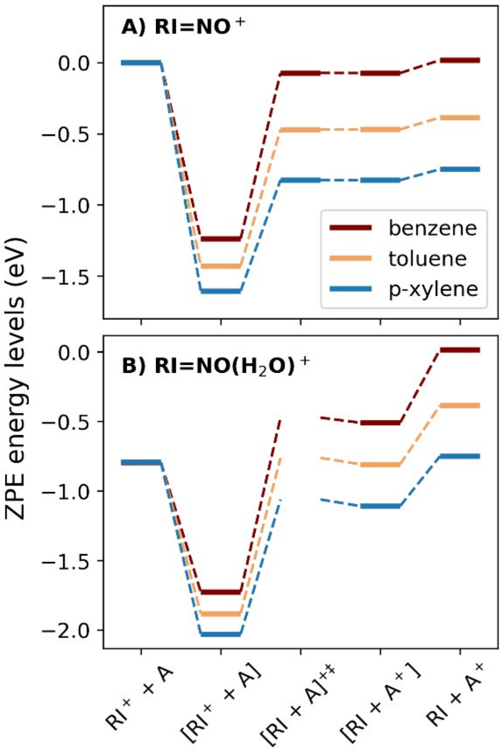

Figure S11: Computed zero-point energy levels for the reactants, products, and intermediate reaction complexes of proton transfer from NO⁺ and NO⁺(H₂O) with benzene, toluene, and p-xylene. Transition states in A) correspond to the MECP of the singlet and triplet surface.

Section S4. Modelled Reaction Rate Coefficients

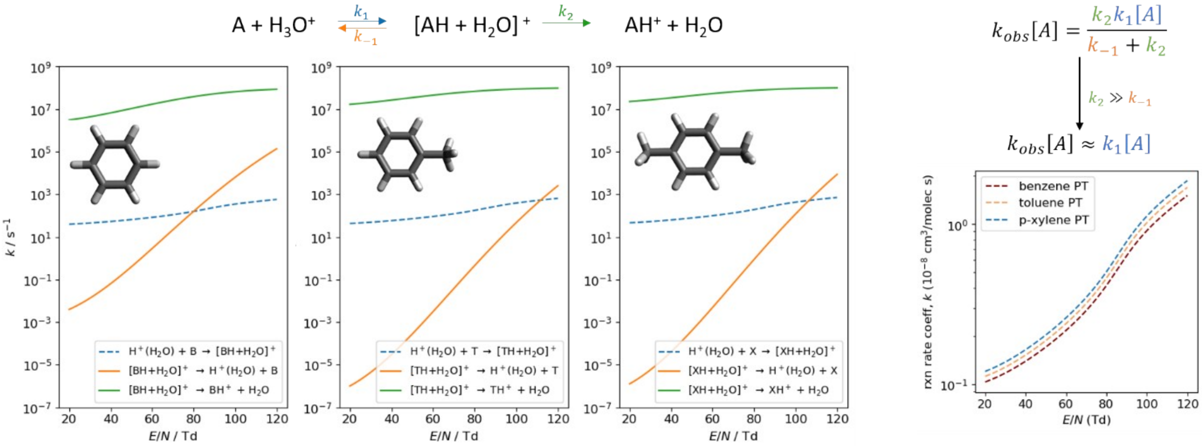

Figure S12: Computed reaction rates (as a function of E/N) for the proton transfer reaction of H_3O^+ with the model analytes.

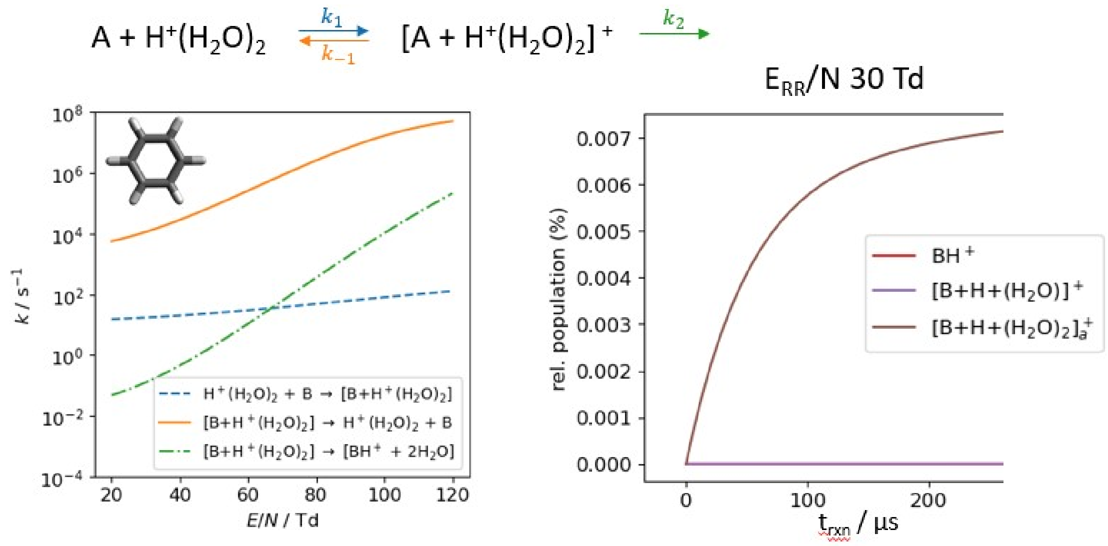

Figure S13: Left: Computed rate coefficients for the proton transfer of $H_3O^+(H_2O)$ to benzene. Evidently, the forward rate coefficient k_2 is not exceeding the reverse rate coefficient k_{-1}. Right: Simulated reaction progress at 30 Td. Instead of forming the protonated analyte, the reaction complex is stable enough to accumulate.

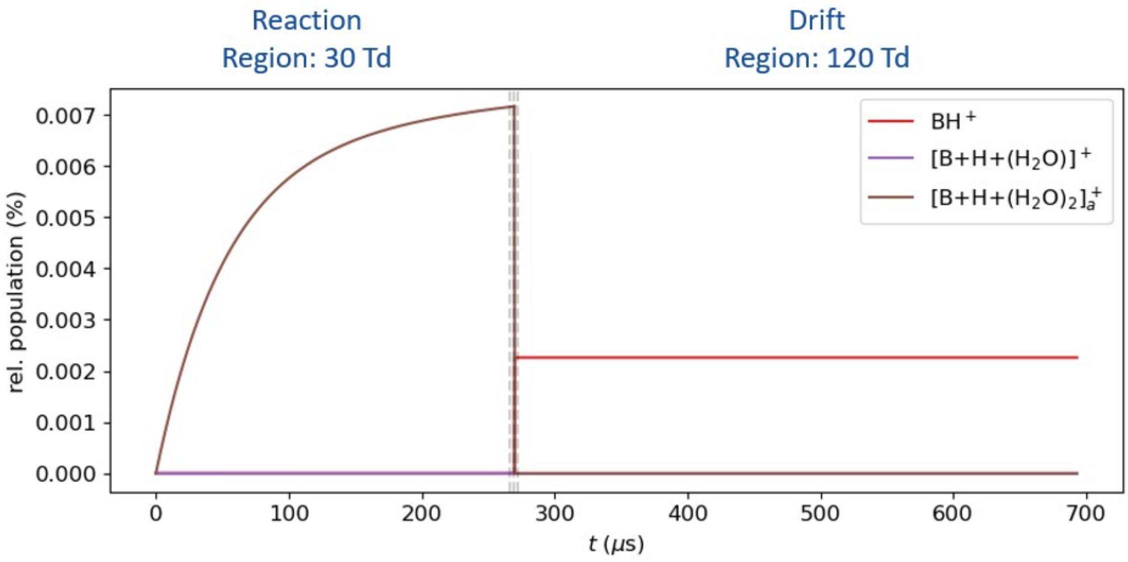

Figure S14: Simulated reaction progress at 30 Td in the reaction region but including the drift region. Through the stability of the reaction complex $[B{+}H^+(H_2O)_2]$, it is predominantly formed in the reaction region without dissociation to the final products. This only occurs in the drift region with a certain branching ratio. Note that the red line is lower than the brown line, meaning that only a portion of the reaction complex reacted towards the products, while the rest reacted back to the reactants.

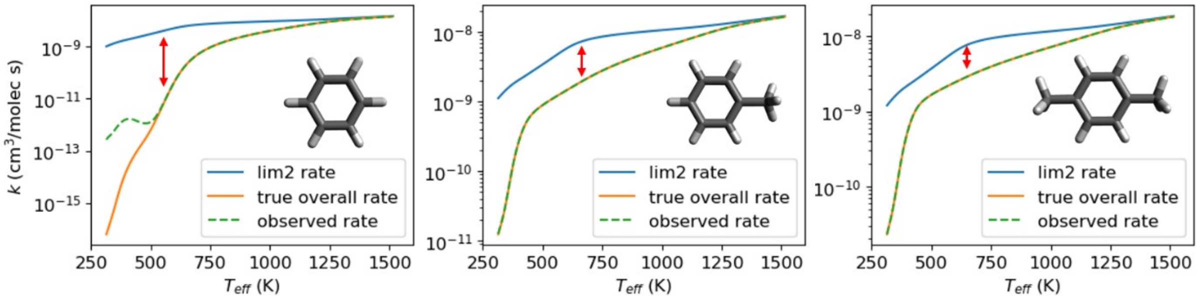

Figure S15: Comparison of modelled proton transfer rates. The limit 2 rate coefficients describe the rate coefficients that would be obtained by direct proton transfer from H_3O^+ in the collision limit. The true overall rate coefficients takes into account the full reaction scheme incl. hydration, but at the end of the reaction region. It necessarily lies below the limit 2 rate coefficients. The observed rate coefficients are the same but are calculated including the drift region.

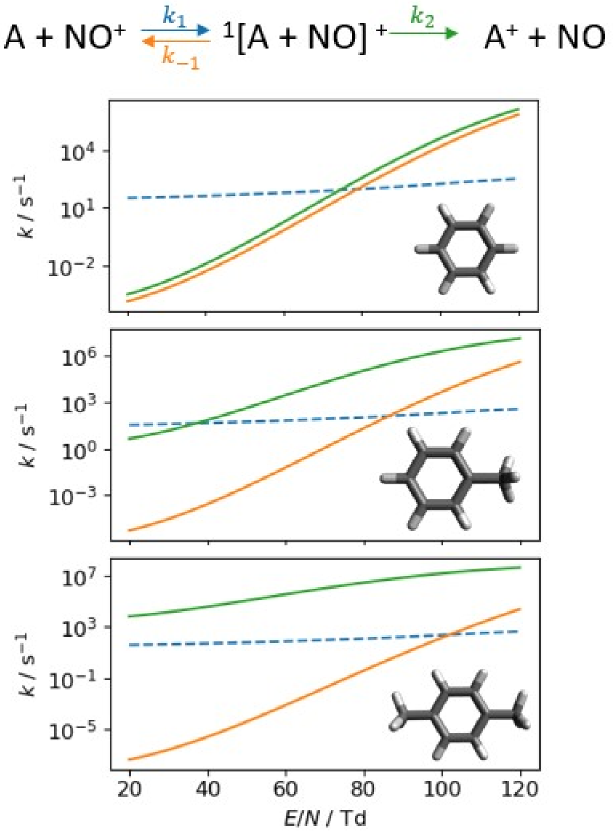

Figure S16: Computed reaction rates (as a function of E/N) for the charge transfer reaction of NO⁺ with the model analytes.

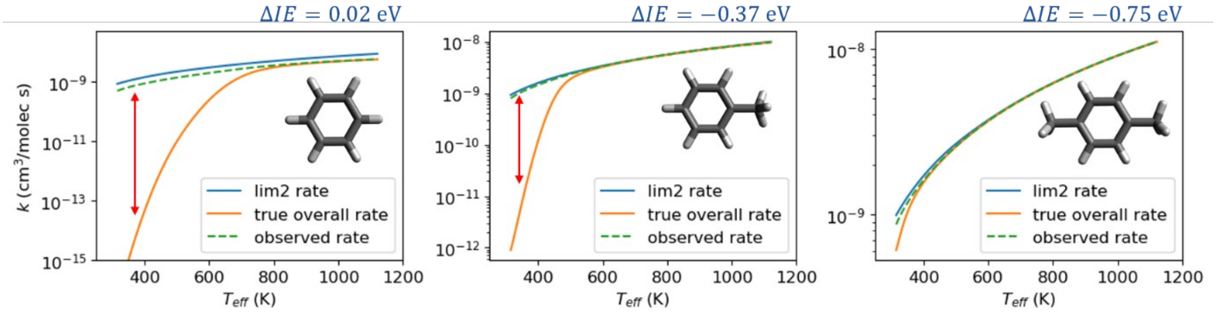

Figure S17: Comparison of modelled charge transfer rates. The limit 2 rate coefficients describe the rate coefficients that would be obtained by direct charge transfer from NO⁺ in the collision limit. The true overall rate coefficients takes into account the full reaction scheme incl. hydration, but at the end of the reaction region. It necessarily lies below the limit 2 rate coefficients. The observed rate coefficients are the same but are calculated including the drift region.

Section S5. Details on Reaction Rate Coefficient Calculations

The expressions for the high-pressure limit rate constants used read:

$$k_{tight} = \kappa \frac{k_B T Q_{TS}^{rv}}{h \; Q_M^{rv}} \exp\left(- \frac{\Delta\varepsilon_0}{k_B T} \right)$$

$$k_{ass}^{'} = \kappa \frac{k_B T}{h} \left(\frac{h^2}{2\pi\mu k_B T} \right)^{3/2} \frac{Q^*}{Q_{neut}^{r}}$$

$$k_{diss} = \kappa \frac{k_B T Q_M^{rv} Q_{neut}^{v} Q^*}{h \; Q_{M-neut}^{rv}} \exp\left(- \frac{\Delta\varepsilon_0}{k_B T} \right)$$

Here, k_B and h are Boltzmann's and Planck's constants, respectively, T is the temperature (see below for discussion), κ is the transmission coefficient and set to ½, μ is the reduced mass of the ion-neutral pair, $\Delta\varepsilon_0$ are zero-point energy corrected threshold energies, Q are rotational (r), or vibrational (v) partition functions of the ion (Q_M), the neutral (Q_{neut}). Q^* is the centrifugal barrier partition function and is n general:

$$Q^* = \sum_{j,k,m,l} \exp\left(- \frac{\varepsilon_{barr}(j,k,m,l)}{k_B T} \right)$$

Where j,k,m are the rotational quantum numbers of the neutral (assuming a symmetric/symmetrized top) and l is the rotational quantum number of the ion-neutral complex. This expression is modelled using the SACM approach, where we differentiate between an ion-induced dipole (IID) potential (e.g., for H_3O^+ interacting with benzene), and an ion-dipole (ID) potential (e.g., H_3O^+ interacting with H_2O), depending on which potential is stronger. The expressions then read:

$$Q_{IID}^* = \frac{\sqrt{2\pi\mu^2 \alpha q^2 k_B T}}{\hbar^2} \cdot Q_{neut}^{r}$$

$$Q_{ID}^* = \frac{2\mu q \mu_D}{\hbar^2} \sum_{j,k,m} \exp\left(- \frac{B_{eff}}{k_B T} \right) \times \int_0^1 \exp\left(- \frac{B_{2D}(2j - |m+k| + 1)^2}{2(1-G) k_B T} \right) dG$$

$$B_{eff} = (B_{1D} - B_{2D}) k^2 + B_{2D} \left[km + \frac{3(k-m)^2 - 3 - (2j - |m+k| + 1)^2}{8} \right]$$

Here, q is the ion's charge, α is the neutral's polarizability, μ_D is the neutral's dipole moment, and B_{1D} and B_{2D} are the rotational constants along and orthogonal to the dipole moment axis of the neutral, respectively, assuming a symmetric/symmetrized top. For more details, see.[5,6]

The temperature enters these equations directly as well as through the temperature dependency of partition functions. As the high reduced electric fields in this work alter the ion temperatures, adaptation of the above equations is warranted. If ions are heated to a specific effective temperature, both k_{tight} and k_{diss} should be evaluated at this T_{eff}, including the partition functions therein. The necessary drift velocities v_D and, correspondingly, the effective temperatures T_{eff} are determined using MobCal-MPI 2.0.[7] For k_{ass}, which actually is just a capturing rate coefficient, the relative collision velocity between the ion and the neutral is most important. For a given drift velocity v_D of the ion, the relative collision velocity can still be described by a temperature, namely:

$$T^{M-neut}_{eff} = T_{bath} + \frac{m_{neut}}{3k_B}(v_D)^2 \frac{m_M + m_{N_2}}{m_M + m_{neut}}$$

Consequently, k_{ass} should be evaluated at this temperature, except Q^{r}_{neut}, as the rotation of the neutral are unaffected by the field and thus thermal. This was already described previously.[6]

Section S6. Relative Peak Areas Depending on E/N

To determine the reaction rate coefficients, the neutral vapor concentration, reaction times and intensities of reactant and product ions are required. The reaction times, *i.e.*, the residence times of H_3O^+ and NO^+ in the reaction region depending on *E/N*, are shown in the main manuscript. To determine the intensities of reactant and product ion, the three model analytes are introduced into the reaction region with a constant vapor concentration of 200 ppb_V and the *E/N* is varied between 20 Td and 120 Td in steps of 1 Td. The relative peak areas shown in Figure S18 are determined from fitting a Gaussian to the peaks in the ion mobility spectra. As can be seen for the proton transfer, no significant product ions can be found at low *E/N*, since the three model analytes are not efficiently ionised by the available large hydrates of the reactant ions. When $H_3O^+(H_2O)$ is formed, the relative peak areas for the protonated monomers of toluene and *p*-xylene increase, whereas the relative peak area for the protonated monomer of benzene only increases when H_3O^+ is formed.

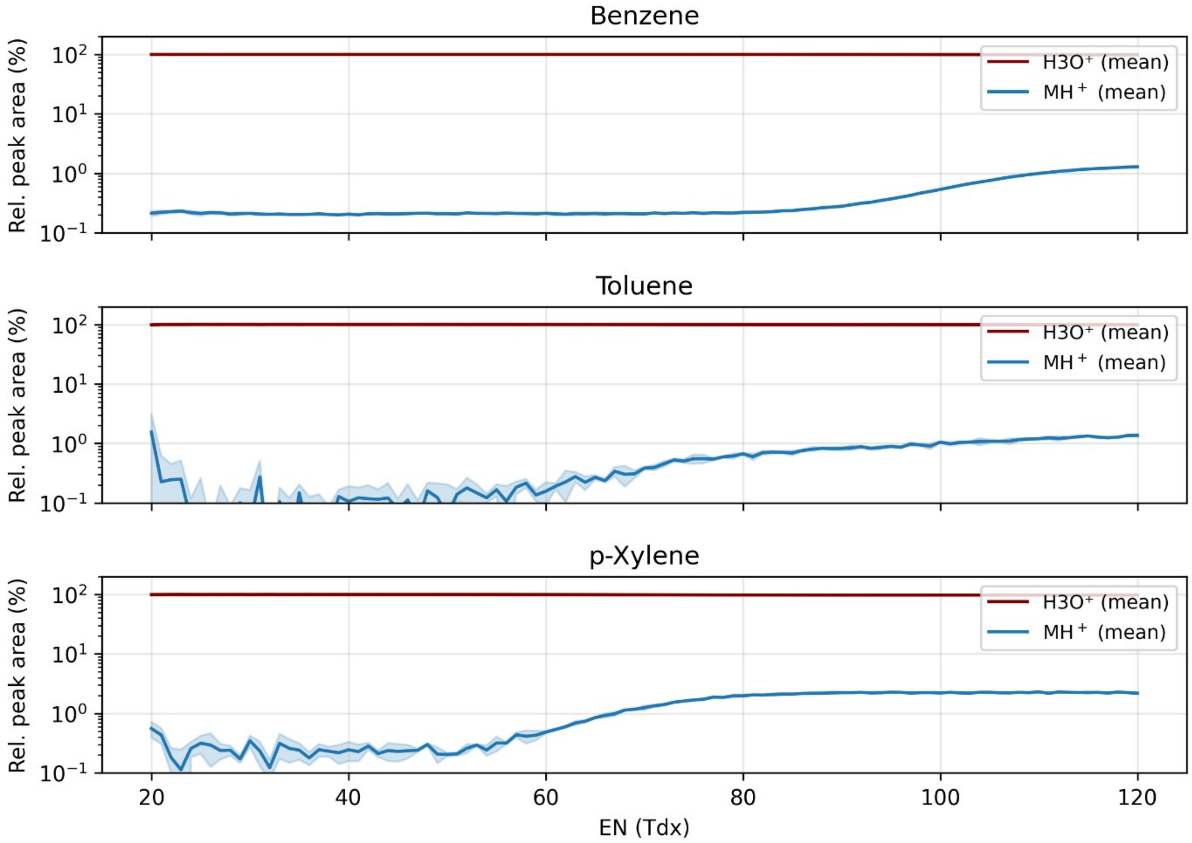

Figure S18: Relative peak areas for $H_3O^+(H_2O)_n$ and the protonated monomer of benzene, toluene and p-xylene depending on reduced reaction field strength.

In contrast to the protonated monomers, the radical cations of the three model analytes are formed at all set values of *E/N* (see Figure S19). As the product ions are formed under all set *E/N* values and the obtained reaction rate coefficients (see main manuscript) are in the same order of magnitude in the investigated range of *E/N*, the relative peak areas of the radical cations steadily decrease due to the decreasing reaction time when increasing *E/N*. Note that this effect is corrected for when determining the reaction rate coefficients.

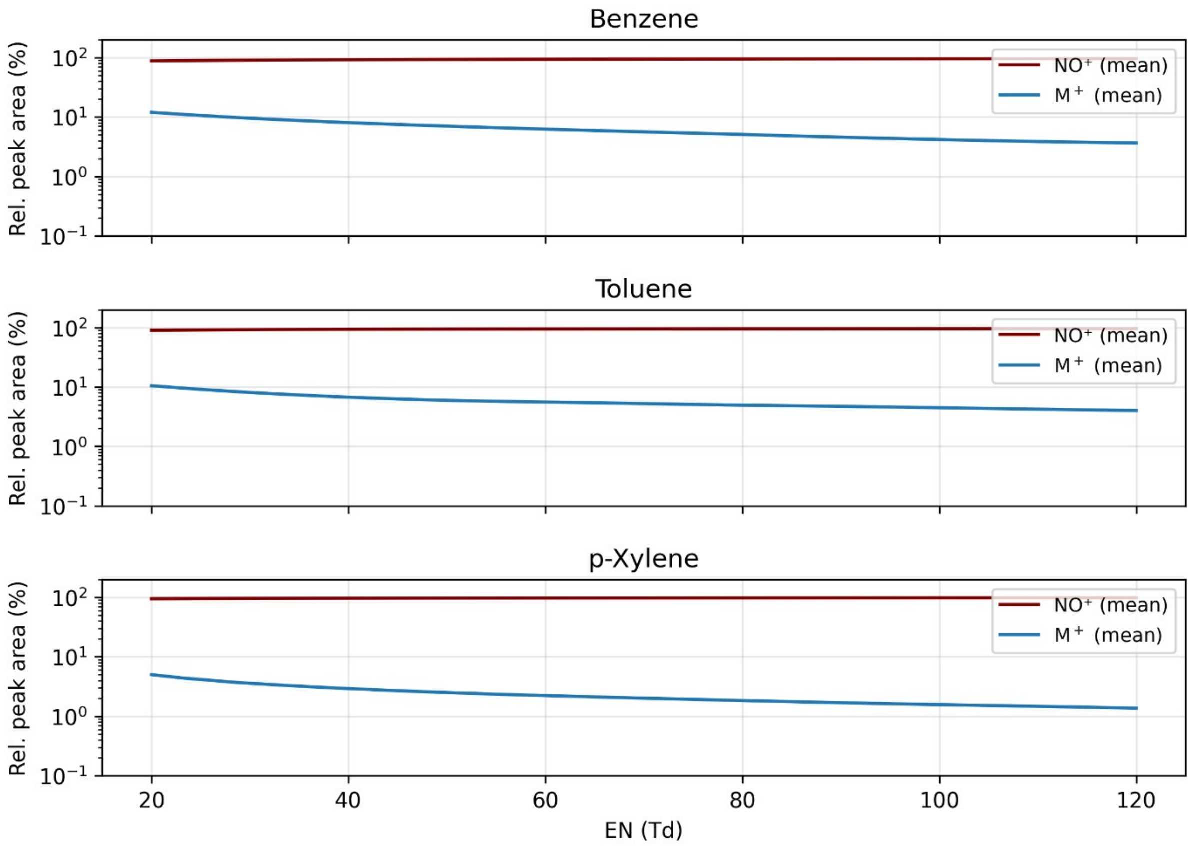

Figure S19: Relative peak areas for $NO^+(H_2O)_m$ *and the radical cations of benzene, toluene and p-xylene depending on reduced reaction field strength.*

Section S7. Radial Diffusion Estimation

Radial diffusion in the drift region was estimated using a standard IMS transport framework based on the Nernst–Einstein relation and the determined effective temperatures. The transverse diffusion coefficient is

$$D_T = \frac{K\,k_B\,T_T}{q},$$

where K is the ion mobility, T_T the transverse ion temperature, k_B the Boltzmann constant and q the elementary charge. The drift time for ions traversing the drift length L under an electric field E is

$$t = \frac{L}{KE}.$$

The radial diffusion width after the drift time is then:

$$\sigma_r = \sqrt{2D_T t} = \sqrt{\frac{2k_B T_T L}{qE}}.$$

The transverse temperatures T_T used for this analysis were obtained according to Mason, McDaniel.[8] For context, the effective ion temperature relates to the longitudinal and transverse temperatures by

$$T_{eff} = \frac{1}{3}T_L + \frac{2}{3}T_T,$$ so that $T_T < T_{eff}$ under our conditions.

Thus, diffusion estimates based purely on T_{eff} represent upper-bound approximations, and the transverse-temperature-based values reported here are more accurate. For the ions with the largest expected diffusion (H_3O^+ and NO^+), the calculated transverse diffusion coefficients yield radial diffusion lengths

$$\sigma_{r,H3O+} < 1.64\ mm; \sigma_{r,NO+} < 1.39\ mm$$

across all relevant operating conditions. Given the drift-tube radius of 21 mm, the diffusion length is more than an order of magnitude smaller than the tube dimensions. Wall collisions caused by radial diffusion are therefore negligible, and differences in σ_r between reactant and product ions should not lead to measurable species-dependent transmission differences under the present operating conditions.

References

1 F. Schlottmann, A. T. Kirk, M. Allers, A. Bohnhorst and S. Zimmermann, High Kinetic Energy Ion Mobility Spectrometry (HiKE-IMS) at 40 mbar, *J. Am. Soc. Mass Spectrom.*, 2020, **31**, 1536–1543.

2 A. Bohnhorst, A. T. Kirk and S. Zimmermann, Simulation aided design of a low cost ion mobility spectrometer based on printed circuit boards, *Int. J. Ion Mobil. Spectrom.*, 2016, **19**, 167–174.

3 M. Allers, A. T. Kirk, C. Schaefer, D. Erdogdu, W. Wissdorf, T. Benter and S. Zimmermann, Field-Dependent Reduced Ion Mobilities of Positive and Negative Ions in Air and Nitrogen in High Kinetic Energy Ion Mobility Spectrometry (HiKE-IMS), *J. Am. Soc. Mass Spectrom.*, 2020, **31**, 2191–2201.

4 A. Haack, C. Schaefer, S. Zimmermann and W. S. Hopkins, Validation of Field-Dependent Ion-Solvent Cluster Modeling via Direct Measurement of Cluster Size Distributions, *J. Am. Soc. Mass Spectrom.*, 2023, **34**, 1035–1046.

5 J. Troe, Statistical adiabatic channel model for ion–molecule capture processes. II. Analytical treatment of ion–dipole capture, *J. Chem. Phys.*, 1996, **105**, 6249–6262.

6 A. Haack and W. S. Hopkins, Kinetics in DMS: Modeling Clustering and Declustering Reactions, *J. Am. Soc. Mass Spectrom.*, 2022, **33**, 2250–2262.

7 A. Haack, C. Ieritano and W. S. Hopkins, MobCal-MPI 2.0: an accurate and parallelized package for calculating field-dependent collision cross sections and ion mobilities, *Analyst*, 2023, **148**, 3257–3273.

8 E. A. Mason and E. W. McDaniel, *Transport Properties of Ions in Gases*, Wiley, 1988.